

See discussions, stats, and author profiles for this publication at: <https://www.researchgate.net/publication/253342684>

# Automated video enhancement from a stream of atmospherically-distorted images: The lucky-region fusion approach

Article in *Proceedings of SPIE - The International Society for Optical Engineering* · August 2009

DOI: 10.1117/12.828332

CITATIONS

60

READS

775

4 authors, including:



**Mathieu Aubailly**

University of Maryland, College Park

22 PUBLICATIONS 110 CITATIONS

[SEE PROFILE](#)



**Mikhail Vorontsov**

University of Dayton, School of Engineering,

334 PUBLICATIONS 3,897 CITATIONS

[SEE PROFILE](#)



**Gary W. Carhart**

Army Research Laboratory

66 PUBLICATIONS 1,203 CITATIONS

[SEE PROFILE](#)

Some of the authors of this publication are also working on these related projects:



Development of a system for forming laser beams with controllable spatial structure for wireless optical communications [View project](#)



AFOSR MURI: Wave Optics of Deep Atmospheric Turbulence: From Underlying Physics towards Predictive Modeling, Mitigation and Exploitation [View project](#)

# Automated video enhancement from a stream of atmospherically-distorted images: the lucky-region fusion approach

Mathieu Aubailly<sup>\*a</sup>, Mikhail A. Vorontsov<sup>a,b</sup>, Gary W. Carhart<sup>b</sup>, Michael T. Valley<sup>c</sup>

<sup>a</sup>University of Maryland, Intelligent Optics Laboratory, College Park, MD USA, 20740;

<sup>b</sup>Army Research Laboratory, Intelligent Optics Laboratory, Adelphi, MD USA 20783;

<sup>c</sup>Sandia National Laboratories, Albuquerque, NM USA 87185

## ABSTRACT

An automated video enhancement technique capable of image fusion from a stream of randomly-distorted images of a still scene is presented in this paper. The technique is based on the “lucky-region” fusion (LRF) approach and aims to improve locally the image quality according to the following steps: (1) for each image of the video stream an image quality map (IQM) which characterizes locally the image quality is computed, (2) each IQM is compared to that of the current fused image leading to the selection of best quality regions (the “lucky-regions”), and (3) the selected regions are merged into the fused video stream. While the LRF approach succeeds in producing images with significantly improved image quality compared to the source images, its performance depends on the imaging conditions and requires adjustment of its fusion parameter – the fusion kernel size – in order to adapt to an evolving environment (e.g. a turbulent atmosphere). Parameter selection was so far performed manually using a trial-and-error approach which causes the technique to be impractical for a real world implementation. The automated LRF technique presented is relaxed from this requirement and selects automatically the fusion parameter based on the analysis of the source images making it more suitable for practical systems. The improved LRF technique is applied to imaging through atmospheric turbulence for various imaging conditions and scenes of interest. In each case automatically-fused video streams demonstrate increases in image quality comparable to that obtained with manual selection of the fusion parameter.

**Keywords:** Image/video fusion, automated processing, image quality map, imaging through turbulence

## 1. INTRODUCTION

Image fusion from multiple frames generally refers to the integration of multisensor data of various spectral, spatial and temporal resolutions and typically aims to sharpen images, enhance specific features, improve classification, or increase registration accuracy<sup>1-15</sup>. While most fusion techniques are developed assuming that variations within the set of source frames are predominantly sensor-originated (e.g. sensors with different spatial and spectral resolutions as it is commonly the case in satellite imaging<sup>1,2,5</sup>), less research efforts are directed toward the fusion of data produced by single image sensors (typically with fixed spectral and spatial resolutions) and where collected images are distinct from each other as a result of random fluctuations of the imaging medium. Common examples of random media are the Earth atmosphere or a turbulent volume of water which cause image sensors to yield time-varying spatially-distorted image data.

A number of image processing techniques that aim to compensate for imaging medium-induced distortions can be found in literature<sup>16-21</sup>. These techniques were typically developed for astronomical applications and assume the distortions introduced by the random medium are independent of position in the image plane (isoplanatic condition). This assumption causes them to fail for a field-of-view (FOV) broader than the isoplanatic angle approximately<sup>22</sup> (anisoplanatic conditions). Under such conditions, few software-based techniques successfully mitigate image distortions. Among them, image restoration techniques based on local shift removal<sup>16,17</sup> are notable but have the downfall to be computationally expensive. Another approach referred to as “lucky-frame” selection<sup>18,19</sup> consists in selecting the best quality frames in a stream of randomly distorted images using an image quality metric. The problem with this approach is the low probability of appearance of a good quality image under anisoplanatic conditions.

<sup>\*</sup>mathieu@umd.edu; phone 1-301-403-8353.

An approach referred to as “lucky-region” fusion<sup>11-15</sup> consists in selecting and fusing image regions with best image quality (the “lucky-regions”) within a set of source images. Lucky-regions are selected using image quality maps (IQMs) which characterize locally the image quality<sup>11,12</sup>. The LRF technique overcomes shortfalls of previously mentioned approaches and succeeds even under anisoplanatic conditions. However, a downside of the method is inherent to its need to manually select its key parameter – the fusion kernel size – in accordance with the fluctuations of the imaging medium. This limitation causes robustness issues and makes the technique impractical for implementation into a real system evolving in a changing environment.

In this paper, we present a method for automated selection of the LRF parameter based on the analysis of the source images. The technique is illustrated with the fusion of atmospherically-distorted experimental data sets and demonstrates image quality improvements using the automated approach comparable to that obtained with manual selection of the parameter.

This paper is organized as follow. The lucky-region fusion technique is first reviewed in Section 2 and the effect of fusion parameter is described. The strategy used to automate the LRF technique is presented in Section 3 and we explain how fusion is performed on video streams of distorted images in Section 4. In Section 5 the automated fusion technique is applied to atmospherically-distorted video streams and fusion results are presented. Section 6 provides concluding remarks.

## 2. LUCKY-REGION FUSION TECHNIQUE

### 2.1 Image quality map

Image quality maps characterize locally the quality of images<sup>11-12</sup> and are used in the LRF technique in order to select lucky-regions within a set of distorted images. An IQM  $M(\mathbf{r})$ , where vector  $\mathbf{r} = \{x, y\}$  denotes the spatial coordinates, is defined as the convolution result between a spatially-varying image quality metric  $J(\mathbf{r})$ <sup>23-25</sup> and a Gaussian kernel  $G(\mathbf{r}, a)$ :

$$M(\mathbf{r}) = \int J(\mathbf{r}') G(\mathbf{r} - \mathbf{r}', a) d^2 \mathbf{r}', \quad (1)$$

where  $G(\mathbf{r}, a) = \exp[-(x^2 + y^2)/a^2]$  and  $a$  is a scalar referred to as the kernel size. The IQM quantifies the image quality within a local region of radius  $a$  centered on point  $\mathbf{r}$ . A commonly used image quality metrics  $J(\mathbf{r})$  based on the image gradient<sup>23-25</sup> is given as

$$J(\mathbf{r}) = \frac{|\nabla I(\mathbf{r}, t)|}{\int I(\mathbf{r}, t). d\mathbf{r}}, \quad (2)$$

where  $\nabla$  denotes the gradient vector operator and  $I(\mathbf{r}, t)$  an image taken at time  $t$ . Note that in order to obtain an image quality metric independent of the overall image intensity Eq. (2) features the integral of the image intensity over the entire image as a normalization factor.

### 2.2 Anisotropic evolution equation

The lucky-region fusion process is based on the following form of the evolution equation<sup>12</sup>:

$$\frac{\partial I_F(\mathbf{r}, t)}{\partial t} = -\Delta(\mathbf{r}, t)[I_F(\mathbf{r}, t) - I(\mathbf{r}, t)], \quad (3)$$

where  $I_F(\mathbf{r}, t)$  denotes the fused image and  $\Delta(\mathbf{r}, t)$ , referred to as the normalized *anisotropic gain*, is given by  $\Delta(\mathbf{r}, t) = \delta(\mathbf{r}, t) / \max_{(\mathbf{r}, t)}[\delta(\mathbf{r}, t)]$  with

$$\delta(\mathbf{r}, t) = \begin{cases} M(\mathbf{r}, t) - M_F(\mathbf{r}, t) & \text{if } M(\mathbf{r}, t) > M_F(\mathbf{r}, t), \\ 0 & \text{otherwise} . \end{cases} \quad (4)$$

$M(\mathbf{r}, t)$  and  $M_F(\mathbf{r}, t)$  denote the IQM's corresponding to images  $I(\mathbf{r}, t)$  and  $I_F(\mathbf{r}, t)$  respectively. The gain  $\Delta(\mathbf{r}, t)$  controls the weight associated with the image region being fused during the LRF process. Note in Eq. (4) that this weight is related to the local image quality improvement with respect to the current fused image. This ensures the fused image  $I_F(\mathbf{r})$  incorporates regions with the best image quality within the set of source images.

### 2.3 Lucky-region fusion technique implementation

Consider the fusion of a set of  $N$  randomly-distorted images of a stationary scene taken at sequential times  $t_n$  denoted  $\{I_n(\mathbf{r})\}$ . The lucky-region fusion is performed iteratively according to the following rule<sup>13-15</sup>:

$$I_F^{(n+1)}(\mathbf{r}) = [1 - \Delta^{(n)}(\mathbf{r})]I_F^{(n)}(\mathbf{r}) + \Delta^{(n)}(\mathbf{r})I_n(\mathbf{r}), \quad (5)$$

where  $\Delta^{(n)}(\mathbf{r})$  corresponds to the anisotropic gain [see Eq. (4)] at iteration  $n$ . The fusion process is initialized using an arbitrary image  $I_F^{(0)}(\mathbf{r})$ . In practice, typical choices for  $I_F^{(0)}(\mathbf{r})$  are the average image  $\hat{I}(\mathbf{r})$  over the entire data set  $\{I_n(\mathbf{r})\}$ , the first frame of the set  $I_0(\mathbf{r})$ , or the frame within the image set with best overall image quality  $J_{\text{img}}$  as defined by  $J_{\text{img}} = \int J(\mathbf{r})d\mathbf{r}$ .

### 2.4 Tradeoff selective vs. inclusive fusion

Fusion results obtained using Eq. (5) are characterized by their dependence on the fusion parameter  $a$  [see Eq. (1)] which controls the size of the lucky-regions being selected and fused. Choosing a large lucky-region size  $a$  causes the algorithm to incorporate more image information from the set of source images into the fused image, at the risk of including areas with low image quality (“inclusive” fusion) and resulting in poor image quality improvements. On the other end, selecting small lucky-regions provides a better optimization of the local image quality (“selective” fusion) but can result in the apparition of image artifacts. Such artifacts typically consist in edges in the fused image that do not correspond to object features in the scene of interest and that are not induced by the random media distortions (so called “artificial” edges). These are the consequence of selecting lucky-regions with excessively abrupt boundaries. In practice, attempts to use a fixed value for the kernel size usually fail when subject to fluctuations of the imaging medium (e.g. variations of the strength of atmospheric turbulence).

The balance between selective and inclusive fusion had been so far established using a trial-and-error approach: the user adjusts the fusion kernel size parameter  $a$  until the fused image satisfies simultaneously the following two conditions: (1) image quality is optimized and (2) no artificial edge is present in the image. The kernel size value for which both conditions are respected is denoted  $a_{\text{man}}$ .

Figure 1 illustrates the effect of the kernel size on fusion results using an experimental data set of  $N = 100$  randomly-distorted images obtained through atmospheric imaging over a near-ground (less than 3 meters) 250 meters long path and for a field-of-view of  $1.2 \times 10^{-3}$  radian. Fig. 1(a) shows the average image  $\hat{I}(\mathbf{r})$  over the entire image set  $\{I_n(\mathbf{r})\}$  for comparison with the fusion results displayed in Figs. 1(b) to 1(d) for  $a = a_{\text{man}}$ ,  $a = a_{\text{man}}/4$ , and  $a = 4a_{\text{man}}$  respectively. The image fused for  $a = a_{\text{man}}$  in Fig. 1(b) shows a significant improvement in image quality compared to the average source image in Fig. 1(a). Note the artificial edges resulting of an excessively selective fusion ( $a < a_{\text{man}}$ ) [see arrows in Fig. 1(c)]. For an overly inclusive fusion ( $a > a_{\text{man}}$ ) the fused image reveals a poor image quality as showed in Fig. 1(d) (see arrows).

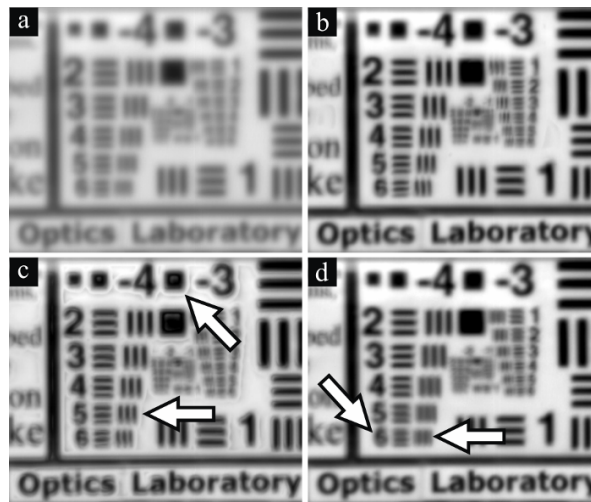


Fig. 1. Fusion results for an experimental set of atmospherically-distorted images using the lucky-region fusion technique with different kernel sizes. Fig. 1(a) shows the source image averaged over the data set and Figs.(b) to (d) display

fusion results for kernel sizes:  $a = a_{\text{man}}$ ,  $a = a_{\text{man}}/4$ , and  $a = 4a_{\text{man}}$  respectively. Note the image quality improvement between source image in Fig. 1(a) and fused image in Fig. 1(b) obtained for  $a = a_{\text{man}}$ . Fig. 1(c) features fusion artifacts due to an excessively selective fusion (see artificial edges as pointed by arrows). Fused image in Fig. 1(d) is characterized by a poor local image quality as a result of an excessively inclusive fusion (see arrows).

### 3. AUTOMATION OF THE LUCKY-REGION FUSION

#### 3.1 Approach

As seen in Section 2, the LRF technique aims to fuse image regions that are characterized by a high spatial frequency content compared to other areas. For this reason the strategy used to select lucky-regions is based on the analysis of the edge content of the source images: for image sets with high frequency content lucky-regions should be picked in a selective manner (i.e. using a small kernel size  $a$ ) and vice versa.

The automation of the LRF technique described in this Section consists in (1) computing an edge metric  $\Gamma$  which characterizes the edge content of the image set  $\{I_n(\mathbf{r})\}$ , and (2) calculating the automated fusion kernel size  $a_{\text{auto}}$  from metric  $\Gamma$  using an experimental model. The model is established in order to comply with the selective/inclusive fusion tradeoff described in Section 2.4.

#### 3.2 Edge metric $\Gamma$

The computation of the edge metric  $\Gamma$  for the set of source images  $\{I_n(\mathbf{r})\}$  is performed according to the following steps:

- *Step 1: jitter compensation*

Random tip/tilt aberrations are the largest contributor to wavefront distortions<sup>26,27</sup> when imaging through atmospheric turbulence. While higher-order aberrations (i.e. defocus, astigmatism, etc.) benefit the LRF by introducing local distortions (mutations) and creating random appearance of high quality regions, tip/tilt aberrations only result in image jitter (i.e. translation). Jitter is compensated during this step for each image of the set with respect to the average image  $\hat{I}(\mathbf{r})$ <sup>28</sup> and the resulting image set is denoted  $\{I_n'(\mathbf{r})\}$ .

- *Step 2: edge map computation*

The average image  $\hat{I}(\mathbf{r})$  yielded by the jitter-compensated image set  $\{I_n'(\mathbf{r})\}$  is used to compute an edge map given as  $\gamma(\mathbf{r}) = |\nabla \hat{I}(\mathbf{r})|$ .

- *Step 3: computation of edge metric  $\Gamma$*

Assuming the edge map  $\gamma(\mathbf{r})$  has a total number of pixels  $N_{\text{pix}}$ , the edge metric  $\Gamma$  is defined as the threshold value for which  $\varepsilon N_{\text{pix}}$  image pixels of  $\gamma(\mathbf{r})$  have a value greater than or equal to  $\Gamma$ . The factor  $\varepsilon \in [0;1]$  is referred to as the *saturation ratio* and is introduced to improve the robustness of metric  $\Gamma$  with respect to edges that are not introduced by random media distortions and that do not correspond to edges in the scene of interest, such as the ones created by dysfunctional camera pixels or dust and scratches on the optics of the imaging system for example. Since the occurrence of such defects is relatively low, we typically set  $\varepsilon$  to a small value in the order of  $10^{-2}$ . Note that for  $\varepsilon = 0$  the metric  $\Gamma$  corresponds to the maximum value of the edge map  $\gamma(\mathbf{r})$  and therefore will be sensitive only to the sharpest edge within the image, however isolated this edge might be.

In practice the edge metric is given by  $\Gamma = h_\gamma[k_e]$  where  $h_\gamma$  is the histogram of edge map  $\gamma(\mathbf{r})$  and  $k_e$  is determine so that

$$\sum_{k=k_\gamma+1}^M h_\gamma[k] < \varepsilon \sum_{k=1}^M h_\gamma[k] \leq \sum_{k=k_\gamma}^M h_\gamma[k], \quad (6)$$

where  $M$  is the number of bins in histogram  $h_\gamma$ .

#### 3.3 Model for the fusion kernel size

In this subsection we substantiate our choice for the model relating the automated kernel size  $a_{\text{auto}}$  to the edge metric  $\Gamma$  defined in Section 3.2. Consider the selection of lucky-regions within an image  $I_G(\mathbf{r})$  consisting of a Gaussian intensity distribution of width  $\sigma > 0$  centered at position  $\mathbf{r}_c$ . The edge metric  $\Gamma$  for image  $I_G(\mathbf{r})$  is derived in the Appendix for  $\varepsilon = 0$  and is given in Eq. (A4) by

$$\Gamma = \frac{1}{\sigma} e^{-1/2}. \quad (7)$$

Furthermore, it is reasonable to assume lucky-regions to be selected in  $I_G(\mathbf{r})$  should correspond to the Gaussian distribution in the image and selection should be performed with kernel size  $a$  directly related to its width  $\sigma$ . Hence, the relation established in Eq. (7) leads us to choose the model between the automated kernel size  $a_{\text{auto}}$  and the edge metric  $\Gamma$  as

$$a_{\text{auto}} = K \frac{1}{\Gamma}, \quad (8)$$

where  $K$  is a calibration factor. Note the relation in Eq. (8) is a model chosen for calculating the fusion parameter  $a_{\text{auto}}$  from image analysis (edge metric) and does not constitute an analytical expression for selecting the fusion kernel size. The calibration of the model is performed experimentally in the next subsection.

### 3.4 Model calibration

The model for the kernel size introduced in Eq. (8) is calibrated (i.e. factor  $K$  is determined) experimentally as follow. Consider  $N_{\text{set}}$  experimental data sets each corresponding to a distinct combination of scenes of interest and imaging conditions (random-distortion strength, imaging distance, light level, etc.). For each data set, the following two steps are performed: (1) the edge metric  $\Gamma$  is computed as shown in Section 3.2, and (2) the LRF technique presented in Section 2 is used to produce multiple fused images from the data set corresponding to kernel sizes within interval  $[a_{\text{min}}, a_{\text{max}}]$  with increments of  $\Delta a$ . The interval is chosen so that  $a_{\text{min}}$  corresponds to a sub-pixel size and  $a_{\text{max}}$  to approximately the size of the image, and increment  $\Delta a$  is chosen in the order of a pixel size. For each set the kernel size  $a_{\text{man}}$  is picked in accordance with criteria established in Section 2.4. Note that kernel size  $a_{\text{man}}$  needs to be user-determined since conventional image quality metrics do not differentiate edges that are inherent to the scene of interest from edges resulting from an excessively small kernel size (artificial edges).

The  $N_{\text{set}}$  resulting data points  $(\Gamma, a_{\text{man}})$  are then fit with the curve corresponding to Eq. (8) in order to minimize the root mean square (RMS) error as illustrated in Fig. 2. A total of  $N_{\text{set}} = 33$  data points corresponding to as many distinct data sets are displayed in the figure for a saturation ratio  $\varepsilon$  of  $10^{-2}$  (see Section 3.2). Curve fitting yields a calibration factor  $K$  of 0.877 and a normalized root mean square error (NRMSE) of 0.191. The relation in Eq. (8) is hence complete and provides a practical way to determine parameter  $a_{\text{auto}}$  from image analysis.

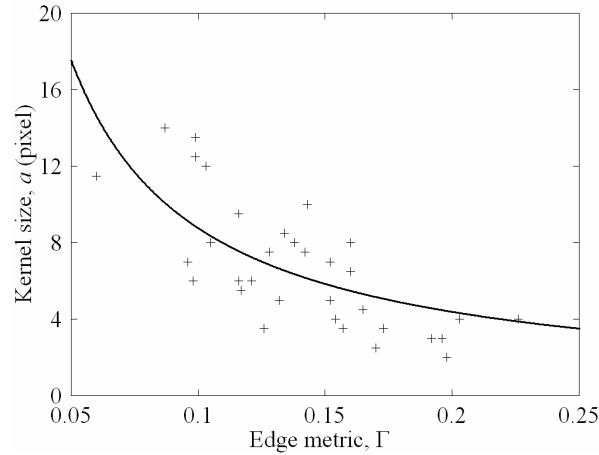


Fig. 2. Plot showing experimental data points  $(\Gamma, a_{\text{man}})$  corresponding to the optimal kernel size for each data set (symbols “+”). The curve corresponds to relation in Eq. (8) and is fit to the data points in the sense of the root mean square error. Curve fitting provides a value for factor  $K$ .

## 4. VIDEO FUSION FROM A STREAM OF IMAGES

The automated LRF technique described in Sections 2 and 3 applies to the fusion of a single image  $I_F(\mathbf{r})$  from a set  $\{I_n(\mathbf{r})\}$  containing a finite number of images taken at sequential times  $t_n$ . However, in many applications image data are captured by a video camera that delivers a stream of images of “infinite” length making the automated LRF technique

introduced earlier impractical. The technique is extended to perform video fusion from a stream of images as follow. Let's denote  $I_m(\mathbf{r})$  a stream of source images taken at sequential times  $t_m$ . An image subset of the video stream corresponding to the temporal window  $[t_{m-N_w+1}, t_m]$  is considered. The subset is denoted  $\{I_m(\mathbf{r})\}_{N_w}$  and contains  $N_w$  sequential images extracted from the "infinite" stream. Images in subset  $\{I_m(\mathbf{r})\}_{N_w}$  are fused into a single frame  $I_{F,m}(\mathbf{r})$  using the LRF technique previously described. The temporal window is then moved forward and the fusion process is repeated sequentially on the next stream subset  $\{I_{m+1}(\mathbf{r})\}_{N_w}$ . Successive frames  $I_{F,m}(\mathbf{r})$  constitute the fused video stream.

## 5. APPLICATION TO ATMOSPHERICALLY-DISTORTED IMAGE SETS AND VIDEO STREAMS

The automated LRF technique is applied to multiple experimental data sets of atmospherically-distorted images collected under various imaging conditions (turbulence strength, imaging distance, etc.) and for different scenes of interest.

A first series of image sets was collected in College Park, Maryland at a near-horizontal 4.2km atmospheric optical path from the Army Research Laboratory similar to the A\_LOT facility<sup>29</sup> on May 1, 2009. The scene of interest consisted of a set of antennas and targets boards imaged with a field-of-view of  $2.8 \times 10^{-3}$  radian. The scene and the imaging system were located at a height of 70 meters (water tower top) and 20 meters above ground respectively. The imaging system consisted in a Celestron C11 telescope with aperture diameter of 280mm and focal length of 2800mm and a Sensor Unlimited camera SU640 collecting  $640 \times 512$  pixels images at a frame rate of 60Hz and for an exposure time of 1.9ms.

The second series of data sets was acquired at the Sandia National Laboratory in Albuquerque, New Mexico in January 2008 over a near-ground propagation path of 1km. The scene of interest consisted in three  $100\text{cm} \times 70\text{cm}$  target boards imaged using a RCOS Ritchey-Chretien telescope with aperture diameter of 315mm and focal distance 2850mm, and a Vision Research Phantom v9 camera producing  $1632 \times 1200$  pixels images corresponding to a FOV of  $2.0 \times 10^{-3}$  radian. Frames were collected at a frame rate of 15Hz with an exposure time of 0.9ms.

The third series of image sets used to illustrate automated LRF was collected at the Army Research Laboratory facility in Adelphi, Maryland on May 11, 2009 and the scene consisted of four human-sized mannequin heads and letter-sized target boards imaged at a distance of 250m with a near-ground (less than 3 meters above ground) propagation path. The imaging system was composed of a telescope Celestron C8 with aperture diameter of 210mm and focal length of 2100mm and a Dalsa CA-D6 camera collecting  $512 \times 512$  pixels images at a frame rate of 86Hz and exposure time of 2.8ms. The full-FOV covered by the imaging system had an angular extend of  $2.2 \times 10^{-3}$  radian.

For each series the number of images  $N$  being fused was established experimentally. The fusion of 100 to 150 frames resulted in significant image quality improvements.

Figs. 3 to 5 show examples of collected data and fusion results corresponding respectively to the three experimental series described above. For each Figure, part (a) shows the average image over the  $N$  images of the set, and parts (b) and (c) show the fused image for automated and manual selection of the fusion kernel size respectively,  $a_{\text{auto}}$  and  $a_{\text{man}}$ . The LRF parameters used are given in Table 1 for each set. For each Figure the fused images in (b) and (c) show a significant improvement in image quality compared to the source image in (a). Also, note the comparable image quality between images fused using the automated and the manual kernel sizes  $a_{\text{auto}}$  and  $a_{\text{man}}$ .

It should be noted that image sets used for illustration in this Section were not utilized during the LRF calibration step described in Section 3.4. This point is essential to demonstrate the technique's independence with regards to source data.

Table. 1. LRF parameters used during the fusion process for three data sets: number of source images being fused  $N$ , manual and automated kernel sizes  $a_{\text{man}}$  and  $a_{\text{auto}}$ .

Data set	#1	#2	#3
Number of images fused, $N$	100	100	150
Fusion kernel size	$a_{\text{auto}}$	6.4 pix.	5.7 pix.
	$a_{\text{man}}$	5.0 pix.	3.5 pix.

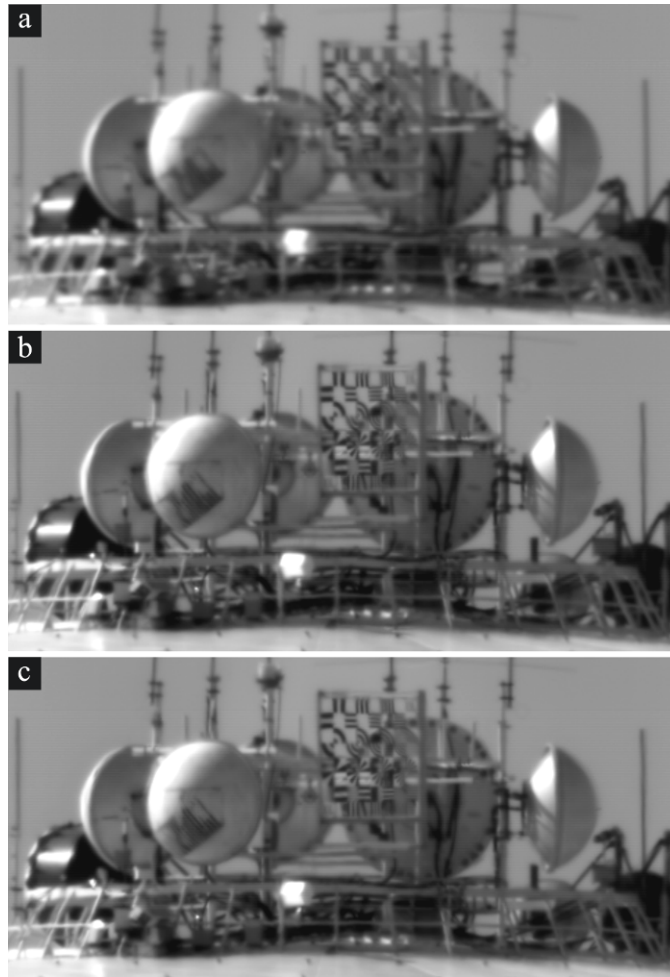


Fig. 3. Imaging results obtained for the first experimental imaging setup: set of antennas and target boards imaged through atmospheric turbulence over a distance of 4.2km. Fig. 3(a) shows the average image over the source data set. Fig. 3(b) and (c) show fusion results for automatically and manually selected kernel sizes respectively:  $a_{\text{auto}} = 6.4$  pixels and  $a_{\text{man}} = 5.0$  pixels. Note the comparable image quality of fused images in (b) and (c).



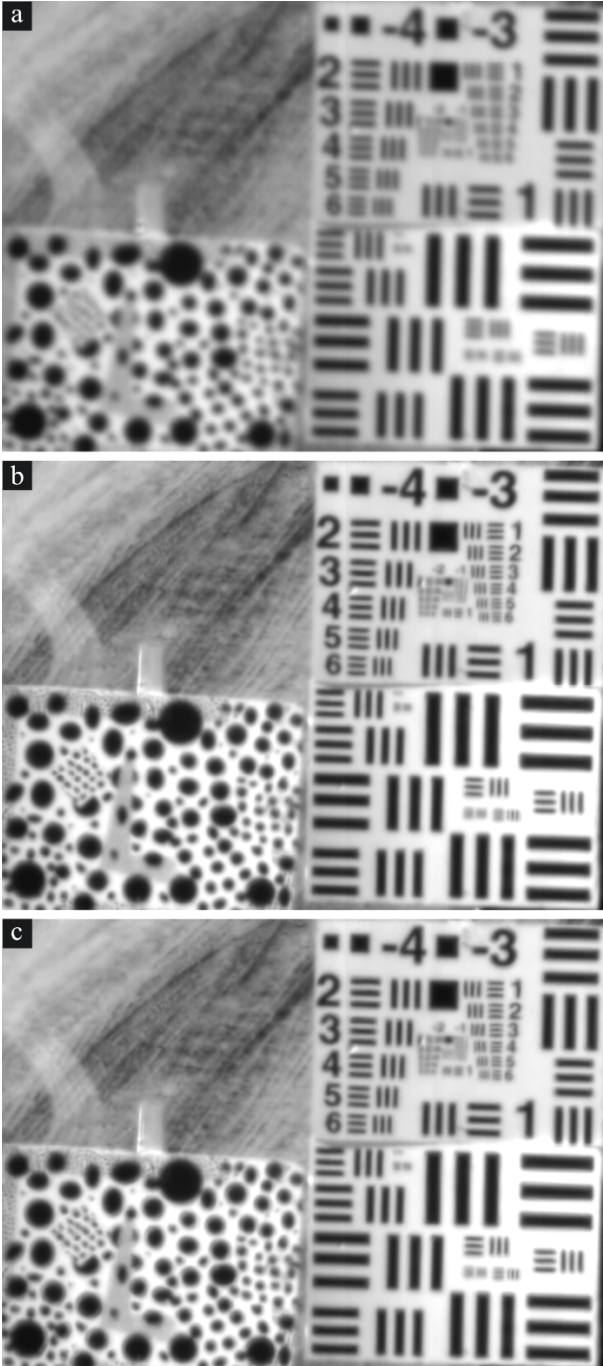


Fig. 4. Imaging results obtained for the second experimental imaging setup: target boards imaged for a near-ground atmospheric propagation path over a distance of 1km. Fig. 4(a) shows the average image over the source data set. Fig. 4(b) and (c) show fusion results for automatically and manually selected kernel sizes respectively:  $a_{\text{auto}} = 5.7$  pixels and  $a_{\text{man}} = 3.5$  pixels. Note the comparable image quality of fused images in (b) and (c).



Fig. 5. Imaging results obtained for the third experimental imaging setup: mannequin head and target boards imaged through near-ground atmospheric turbulence over a distance of 250m. Fig. 5(a) shows the average image over the source data set. Fig. 5(b) and (c) show fusion results for automatically and manually selected kernel sizes respectively:  $a_{\text{auto}} = 6.3$  pixels and  $a_{\text{man}} = 7.0$  pixels. Note the comparable image quality of fused images in (b) and (c).

## 6. CONCLUSION

An improvement to the lucky-region fusion technique was presented. The upgrade consists in automating the LRF technique's most critical fusion parameter: the fusion kernel size. The automation is based on the analysis of the source data and uses an edge metric as well as an experimental model in order to derive the fusion kernel size. The improved LRF technique has the advantage to require no user intervention and allows for LRF implementation into a system operating into a changing environment. In addition, since the automation is based solely on source image analysis there is no need to characterize turbulence strength for example using a scintillometer. Experimental validation of the automated LRF technique is provided with multiple examples and demonstrates fusion results with image quality comparable to that obtained with user selecting manually the kernel size.

## APPENDIX

Consider image  $I_G(\mathbf{r})$  consisting of a Gaussian intensity distribution of widths  $\sigma > 0$  centered at positions  $\mathbf{r}_c$ :  $I_G(\mathbf{r}) = \exp[-|\mathbf{r}-\mathbf{r}_c|^2/(2\sigma^2)]$ , where  $\mathbf{r}_c = \{x_c, y_c\}$ . The first derivative of  $I_G(\mathbf{r})$  with respect to variable  $x$  is given by

$$\frac{\partial I_G(x, y)}{\partial x} = -\frac{x - x_c}{\sigma^2} I_G(x, y), \quad (\text{A1})$$

and its second derivative by

$$\frac{\partial^2 I_G(x, y)}{\partial x^2} = -\frac{1}{\sigma^2} \left[ 1 - \frac{(x - x_c)^2}{\sigma^2} \right] I_G(x, y). \quad (\text{A2})$$

From Eq. (A2), the extrema of  $\frac{\partial I_G(x, y)}{\partial x}$  are reached for

$$x = x_c \pm \sigma. \quad (\text{A3})$$

From Section 3.2, the edge metric  $\Gamma$  for  $N = 1$  is given for  $\alpha = 0$  as  $\Gamma = \max_{\mathbf{r}} \left| \frac{\partial I_G(\mathbf{r})}{\partial \mathbf{r}} \right|$ . From Eqs. (A1) and (A3) we thus have

$$\Gamma = \frac{1}{\sigma} e^{-1/2}. \quad (\text{A4})$$

## ACKNOWLEDGMENTS

The authors thank Konley Aschenbach from the Army Research Laboratory in Adelphi, MD for his technical advices with algorithm coding and Timothy Koehler from the Sandia National Laboratories in Albuquerque, NM for his feedback, comments and suggestions on the automated lucky-region fusion technique.

## REFERENCES

- [1] Pohl, C. and van Genderen, J. L., "Multisensor image fusion in remote sensing: concepts, methods and applications," Int. J. Rem. Sens., 19, 823-854 (1998).
- [2] Schistad-Solberg, A. H., Jain, A. K. and Taxt, T., "Multisource classification of remotely sensed data: fusion and Landsat TM and SAR images," IEEE Trans. Geo. Sci. Rem. Sens., 32, 768-778 (1994).
- [3] Karathanassi, V., Kolokoulis, P. and Ioannidou, S., "A comparison study on fusion methods using evaluation indicators," Int. J. Rem. Sens., 28, 2309-2341 (2007).
- [4] Park, J.-H., Wikantika, K. and Tateishi, R., "Comparison of four different methods to fuse multi-sensor and multi-resolution remotely sensed data for urban topographic mapping," IEEE IGARSS 1999: Proc. of the Int. Geo. and Rem. Sens. Symposium, 2, 1203-1205 (1999).

- [5] Chavez, P. S., Sides, S. C. and Anderson, J. A., "Comparison of three different methods to merge multiresolution and multispectral data: Landsat TM and SPOT panchromatic," *Photogramm. Eng. Rem. Sens.*, 57, 295-303 (1991).
- [6] Zheng, S., Shi, W.-Z., Liu, J., Zhu, G.-X. and Tian, J.-W., "Multisource image fusion method using support value transform," *IEEE Trans. Image Proc.*, 16, 1831-1838 (2007).
- [7] Li, S., Kwok, J. T.-Y., Tsang, I. W.-H. and Wang, Y., "Fusing images with different focuses using support vector machines," *IEEE Trans. Neural Networks*, 15, 1555-1560 (2004).
- [8] Yocky, D. A., "Image merging and data fusion by means of the discrete two-dimensional wavelet transform," *J. Opt. Soc. Am. A*, 12, 1834-1841 (1995).
- [9] Scheunders, P. and De Backer, S., "Fusion and merging of multispectral images with use of multiscale fundamental forms," *J. Opt. Soc. Am. A*, 18, 2468-2477 (2001).
- [10] Leckie, D. G., "Synergism of SAR and visible/infrared data for forest type discrimination," *Photogramm. Eng. Rem. Sens.*, 56, 1237-1246 (1990).
- [11] Carhart, G. W. and Vorontsov, M. A., "Synthetic imaging: nonadaptive anisoplanatic image correction in atmospheric turbulence," *Opt. Lett.*, 23, 745-747 (1998).
- [12] Vorontsov, M. A., "Parallel image processing based on an evolution equation with anisotropic gain: integrated optoelectronic architectures," *J. Opt. Soc. Am. A*, 6, 1623-1637 (1999).
- [13] Vorontsov, M. A. and Carhart, G. W., "Anisoplanatic imaging through turbulent media: image recovery by local information fusion from a set of short-exposure images," *J. Opt. Soc. Am. A*, 18, 1312-1324 (2001).
- [14] John, S. and Vorontsov, M. A., "Multiframe selective information fusion from error estimation theory," *IEEE Trans. Image Proc.*, 14, 577-584 (2005).
- [15] Aubailly, M., Vorontsov, M. A., Carhart, G. W. and Valley, M. T., "Image enhancement by local information fusion with pre-processing and composed metric," *Atmospheric Optics: Models, Measurements, and Target-in-the-Loop Propagation II*, Proc. of SPIE, 7090 (2008).
- [16] Fraser, D., Thorpe, G. and Lambert, A. J., "Atmospheric turbulence visualization with wide-area motion-blur restoration," *J. Opt. Soc. Am. A*, 16, 1751-1758 (1999).
- [17] Fraser, D. and Lambert, A. J., "Wide area image restoration using a new iterative registration method," *Image Reconstruction From Incomplete Data*, Proc. SPIE, 4123, 64-72 (2000).
- [18] Fried, D. L., "Probability of getting a lucky short-exposure image through turbulence," *J. Opt. Soc. Am. A*, 68, 1651-1658 (1978).
- [19] Baldwin, J. E., Tubbs, R. N., Cox, G. C., Mackay, C. D., Wilson, R. W. and Andersen, M. I., "Diffraction-limited 800 nm imaging with the 2.56 m Nordic Optical Telescope," *Astron. and Astrop.*, 368, L1-L4 (2001).
- [20] Roggemann, M. C., Stoudt, C. A. and Welsh, B. M., "Image spectrum signal-to-noise ratio improvement by statistical frame selection for adaptive optics imaging through atmospheric turbulence," *Opt. Eng.*, 33, 3254-3264 (1994).
- [21] Thelen, B. J., Carrara, D. A. and Paxman, R.G., "Fine-resolution imagery of extended objects observed through volume turbulence using phase-diverse speckle," *Propagation and Imaging through the Atmosphere III*, Proc. SPIE, 3763, 102-111 (1999).
- [22] Fried, D. L., "Anisoplanatism in adaptive optics," *J. Opt. Soc. Am. A*, 72, 52-61 (1982).
- [23] Muller, R. A. and Buffington, A., "Real-time correction of atmospherically degraded telescope images through image sharpening," *J. Opt. Soc. Am.*, 64, 1200-1210 (1974).
- [24] Buerkle, A., Schmoekel, F., Kiefer, M., Amavasai, B. P., Caparrelli, F., Selvan, A. N. and Travis, J. R., "Vision-based closed-loop control of mobile microrobots for micro handling tasks," *Microrobotics and Microassembly III*, Proc. of SPIE, 4568 (2001).
- [25] Xydeas, C. S. and Petrovic, V., "Objective image fusion performance measure," *Electron. Lett.*, 36(4), 308-309 (2000).
- [26] Fried, D. L., "Statistics of a geometric representation of wavefront distortion," *J. Opt. Soc. Am.*, 55, 1427-1431 (1965).
- [27] Roggemann, M. C. and Welsh, B. M., [Imaging through turbulence], CRC Press, Boca Raton, Florida (1996).
- [28] De Castro, E. and Morandi, C., "Registration of translated and rotated images using finite Fourier transforms," *IEEE Trans. Pattern Analysis and Machine Intelligence*, 9, 700-703 (1987).
- [29] Vorontsov, M. A., Carhart, G. W., Banta, M., Weyrauch, T., Gowens II, J. and Carrano, J. C., "Atmospheric laser optics testbed (A\_LOT): atmospheric propagation characterization, beam control, and imaging results," *Proc. SPIE, Advanced Wavefront Control: Methods, Devices, and Applications*, 5162, 37-48 (2003).